Soft Matter

PAPER

View Article Online
View Journal | View Issue

Cite this: *Soft Matter*, 2021, **17**, 2942

Exploring secondary interactions and the role of temperature in moisture-contaminated polymer networks through molecular simulations†

Rishabh D. Guha, [a] Ogheneovo Idolor, [a] Katherine Berkowitz,[a] Melissa Pasquinelli [b] and Landon R. Grace *[a]

Received 11th November 2020,
Accepted 4th February 2021

DOI: 10.1039/d0sm02009e

rsc.li/soft-matter-journal

Leveraging the state of absorbed moisture within a polymer network to identify physical and chemical features of the host material is predicated upon a clear understanding of the interaction between the polymer and a penetrant water molecule; an understanding that has remained elusive. Recent work has revealed that a novel damage detection method that exploits the very low baseline levels of water typically found in polymer matrix composites (PMC) may be a valuable tool in the composite NDE arsenal, provided that a clear understanding of polymer–water interaction can be obtained. Precise detection, location, and possible quantification of the extent of damage can be performed by characterizing the physical and chemical states of moisture present in an in-service PMC. Composite structures have a locally elevated dielectric constant near the damage sites due to a higher fraction of bulk ("free") water, which has a higher dielectric constant when compared to water molecules bound to the polymer network through secondary bonding interactions. In this study, we aim to get a clear atomistic scale picture of the interactions which drive the dielectric signature variations necessary for tracking damage. Molecular Dynamics (MD) simulations were used to explore the effect of temperature on the state of moisture in two epoxy matrices with identical chemical constituents but different morphologies. The motivation was to understand whether higher polarity binds a greater fraction of moisture even at higher temperatures, leading to suppressed dielectric activity. Consequently, the influence of secondary bonding interactions was investigated to understand the impact of temperature on the absorbed water molecules in a composite epoxy matrix.

1. Introduction

Epoxy-based polymers are widely and increasingly used in the automotive and aerospace sectors as the matrix material in polymer matrix composites (PMC).[1,2] The continuous demand for improved performance in these sectors is expected to drive growth in the global composite market to over 146 billion USD by 2026.[3] This expansion is primarily driven by the fact that composites offer superior strength to weight ratio,[4] resistance to chemical contamination,[5] thermal stability, and better electrical insulation properties,[6] when compared to conventional materials. Owing to their electrically insulating properties, epoxies have a low dielectric constant, making them the primary material of choice for aircraft and automotive structures requiring high electromagnetic signal transparency, such as radomes.[2]

However, signal transmissivity is often degraded due to low levels of water absorption from periodic precipitation or moisture present in ambient air. Epoxies can absorb between 1–7% of moisture by weight.[7] This sensitivity to moisture absorption serves as a major source of degradation in the overall performance of polymer composites.[2,4,8,9] Since these materials readily absorb moisture in wet or humid environments[9,10] and are also frequently subjected to cycles of extreme temperature variation and humidity,[1,11] the degradation is generally unavoidable despite advances in coating methods and materials. As a result, there is typically a marked impact on the mechanical performance and thermal stability of epoxy matrices as the moisture plasticizes the matrix and lowers the glass-transition temperature (T_g).[1,11–16] It also degrades the electrical insulation properties; the extent and impact of which is crucial for radome applications where the volume, distribution, and state of absorbed water play critical roles in radar transmissivity and performance.[2] The

[a] *Department of Mechanical and Aerospace Engineering, North Carolina State University, Engineering Building-III, 911 Oval Drive, Raleigh, NC-27695, USA. E-mail: lgrace2@ncsu.edu*

[b] *Department of Forest Biomaterials, College of Natural Resources, North Carolina State University, Biltmore Hall, 2820 Faucette Drive, Raleigh, NC-27606, USA*

† Electronic supplementary information (ESI) available. See DOI: 10.1039/d0sm02009e

degradation of fiber–matrix interfaces,[8] delamination,[11,17] matrix swelling,[12] and subsequent generation of micro cracks[4] due to moisture absorption have also been widely reported.

A fundamental understanding of the transport mechanism and interaction behavior of absorbed moisture in an epoxy network can serve as the cornerstone for developing damage detection and mitigation techniques for polymer-based composites as demonstrated in previous work.[9,10,18]

Many experimental studies have been performed using characterization techniques like infrared spectroscopy (NIR, FTIR), Nuclear Magnetic Resonance (NMR), and dielectric relaxation[19–24] to elucidate the behavior of molecular water in a polymer network. Several of these studies[23–33] have posited the theory of two distinct states of absorbed moisture in the network; water molecules can exist as either ''bound'' water participating in extensive secondary bonding (hydrogen bonding, van der Waals interactions) or as ''free'' water molecules in voids, micro-cracks, and other free volume within the network. Quantifying the dual states of moisture in the network is complicated and is dependent on multiple factors including the concentration of absorption,[19,34] chemical morphology, and the physical attributes (free volume, crosslinking density, void concentration) of the particular epoxy network being studied.[35–38]

For example, in a study conducted by Frank *et al.*[39] on epoxy blends with different crosslinking densities, the diffusion coefficient of absorbed water molecules was observed to decrease with increasing crosslink density. They postulated that increasing the crosslinking results in a greater number of polar sites in the network which, in turn, amplifies the tendency of the water molecules to become ''bound'' and contribute to slower diffusion rates. However, an increase in crosslinking also results in a greater availability of fractional free volume (FFV) and multiple studies[7,37–39] have reported that the nature of interactions between the polar sites in the epoxy and the absorbed water molecules is influenced by the availability of free volume. A recent molecular simulation study[40] illustrated that with an initial increase in crosslinking, the diffusion coefficient of the water molecules decreases due to a greater fraction of ''bound'' water. However, at very high crosslinking densities, the greater free volume aids the clustering of water molecules and results in a gradual rise in the diffusion coefficient.

Although there are multiple theories governing the behavior of absorbed moisture in an epoxy network, the phenomenon occurs at an atomic scale. This makes MD simulations a potentially viable method to provide a molecular level picture within crosslinked epoxy networks as evidenced in previous studies.[41–48] MD has been very successful in characterizing non-bonded atomic interactions between different polar species including the variation of the secondary bonding interactions with increasing moisture concentration and its effect on physical properties.[34,49–56] Simulation studies have also been performed to study the evolution of free volume in the epoxy curing process[57] and the characteristics of moisture absorption in epoxy resins with different network structures.[58]

It is evident from previous experimental and computational work that varying the crosslinking density can potentially alter the strength of polar interactions between the network and the absorbed moisture, but the influence of temperature on such interactions is not well understood. Sorption studies of an epoxy resin exhibited hysteresis during desorption, and residual water was removed only after heating the resin beyond 100 °C.[19] A study of the diffusion of moisture in epoxy-glass composites over a range of partial pressure and temperature concluded that the absorption–desorption process in these systems is quasi-reversible and the incomplete removal of the small content of ''bound'' moisture from the network can have a significant effect on moisture reabsorption.[59] Zhou *et al.*[60] described the desorption process with a two-tiered approach. The first tier, called Type-I desorption, occurs at lower temperatures. Type-II desorption of the ''bound'' water with a higher activation energy requires a higher desorption temperature. Lin *et al.*[51] used MD to study desorption behavior by analysing the diffusion coefficients at different temperatures in an epoxy resin and compared the calculated desorption activation energy with experimental results.

In this study, we use MD simulations to investigate how the increase in temperature impacts the interaction characteristics in two moisture contaminated epoxy networks with very different crosslinking densities. The atomic level details provide insight into the phenomenon of intermolecular hydrogen bonding and its quantitative impact on the desorption activation energy of water at different temperatures. Finally, the variation of the dipolar characteristics of the water molecules in both networks has been analysed to understand the role of temperature on the dielectric activity of moisture in the epoxy networks.

2. Simulation details

The details of the simulation methodology followed are similar to our previous study,[40] a portion of which are repeated here for convenience. The two constituents of a polymer composite matrix—epoxy and the hardener—are in a highly crosslinked state which imparts the network with the necessary mechanical and thermal stability. In our case, a molecular model of an uncrosslinked system was built using the Amorphous Builder module in the MAPS platform of Scienomics (Materials and Processes Simulations Platform, Version 4.2.0, Scienomics SARL, Paris, France). The system consisted of the epoxy (DGEBA) and the hardener (DETA). The Crosslinker module in MAPS was used to generate systems with different crosslink densities and all MD simulations were executed using the open-source software package, LAMMPS.[61] The Amber Cornell Extension Force Field (ACEFF)[62] was used to describe both the bonded and non-bonded interactions between atoms. The Gasteiger method,[63] which is a type of electronegativity equalization method (EEM) was used to assign partial charges to each atom and for the water molecules the TIP3P model[64] was used. The crosslinker module is based on an algorithm similar to the one followed by Varshney *et al.*[43] Two different systems with varying

crosslink densities were generated and each system was equilibrated using a multi-step annealing approach. Post-equilibration, a fixed number of water molecules were inserted into the two systems to simulate the desired degree of moisture contamination (by wt%).

2.1 Crosslinking procedure

To execute the crosslinking reaction between the epoxy and the hardener molecules, 64 molecules of DGEBA and 32 molecules of DETA were first packed in a simulation cell. The activated DGEBA and DETA molecules used to construct the cell are depicted in Fig. 1. The carbon, hydrogen, oxygen and nitrogen atoms have been represented by grey, white, red and blue colors, respectively.

Care was taken to maintain the 2 : 1 ratio between the epoxy and the hardener molecules because an activated DGEBA molecule is bifunctional with two reaction sites ($-CH_2^+-$) while the DETA molecule is tetrafunctional with four reaction sites ($-N^{2-}-$). Therefore, each molecule of DETA is capable of executing four crosslinking reactions while the DGEBA molecule can execute only two.

In the MAPS crosslinking module, each cycle in the crosslinking process was a combination of a geometry optimization (500 steps), a short *NPT* MD relaxation (5 picoseconds, 1000 steps) and a subsequent 5-step algorithm which creates new bonds based on the distance between reaction centers. At the end of the cycle, if the target crosslinking percentage was achieved, the process was terminated. Using this iterative algorithm, two different systems were obtained with crosslink densities of 20% and 81% respectively. During the crosslinking process, all the molecules involved (DGEBA/DETA) were in the activated state. This was necessary for the execution of the crosslinking reaction, but once the process was completed for a particular crosslinking density, the simulation cell was visualized in MAPS and all the reacted and the unreacted sites were selected. This can be performed through the specific atom-group selection procedure in MAPS. Subsequently the unreacted $-CH_2^+-$ groups were located and a bond was created between $-CH_2^+-$ and the neighbouring oxygen atom. Once all the bonds were formed, the hydrogens in the simulation cell was adjusted so that no atom in the cell was violating its valency. This led to the creation of crosslinked sites which had neighbouring hydroxyl groups (from the crosslinking reaction procedure) and unreacted epoxy rings without any hydroxyl groups (from the bond creation process). The geometry optimization process (described later) was performed next to relax the systems to their equilibrium state. This also led to the optimization of bond lengths in the manually created bonds in the epoxy rings. Since greater crosslinking generates a larger number of polar hydroxyl sites, the first network with the lower crosslinking density was considerably less polar than the second network.

2.2 Simulations prior to moisture contamination

After both the systems were built, their energies were minimized through a 500-step geometry optimization using the Steepest Descent method. In experimental conditions, the curing reaction between epoxy and hardener molecules is performed at elevated temperatures and the reaction products are slowly cooled to a lower temperature in a post-cure process. Similarly, in the crosslinker module, the simulation temperatures are high and it is critical to slowly lower the temperature and equilibrate the cell at that temperature before introducing moisture contamination. A large gradient in temperature in a single simulation will not produce a stable and well-equilibrated cell, especially if the simulation time period is not sufficiently long. Therefore, a multi-step anneal and equilibrate method was followed to sequentially lower the temperature and keep the simulation cell equilibrated. In this method, the temperature of the cell was lowered from 600 K to 300 K in six steps. The periodic boundary conditions (PBC) were imposed on each simulation cell. In each step, the temperature was reduced by 50 K through a 100 picosecond (ps) MD simulation using the constant pressure and temperature (*NPT*) ensemble. After the 100 ps simulation was completed, the cell was equilibrated at that temperature using a short 20 ps *NPT* simulation. The *NPT* ensemble was selected because it allows us to obtain the density of the systems which has been used for validation. In all simulations, the Nose–Hoover barostat with a damping of 350 femtoseconds (fs) and

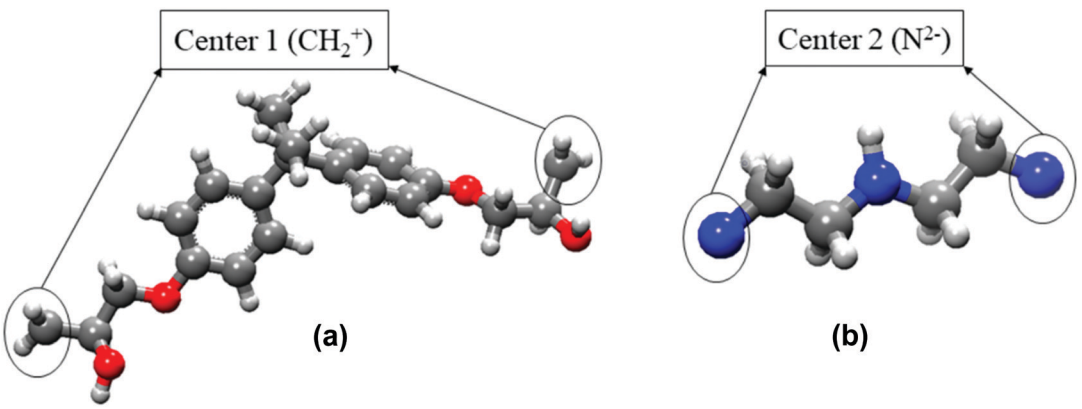

Fig. 1 (a) Activated DGEBA molecule. (b) Activated DETA molecule.[40]

thermostat with a damping of 10 fs were used to control temperature and pressure in the ensemble. The cut-off distance for non-bonded interactions was set at 12 Å and the particle–particle particle-mesh (PPPM) method with an accuracy of 0.0001 was used to calculate the summation of the electrostatic forces. Fig. S1 in the ESI† illustrates the variation in total energy during an annealing and equilibration cycle, respectively. A longer equilibration run of 1 nanosecond (1000 ps) was performed at the final equilibration temperature of 300 K before introducing the water molecules into the systems.

The structure of the dry epoxy networks at different crosslinking densities was rigorously validated in our previous work.[40] The mechanical properties were compared with previous simulation studies and the results were found to be consistent. As a general trend the Young's modulus increased with greater crosslinking densities but there were diminishing gains in stiffness at very high crosslinking. The free volume available in the dry systems was also evaluated and it was found to increase with higher crosslinking.

The T_g of the epoxy matrices is a critical thermomechanical property which conveys information about the temperature range in which an epoxy transitions from a glassy to the rubbery state. Since the study deals with the effect of high temperatures on the molecular interactions between polar molecules like water and the epoxy network, the T_g of our simulated matrices becomes an important parameter. Therefore, for both networks, the T_g was calculated from the specific volume *versus* temperature curve and showed that the glass transition temperature increased with increasing crosslinking density. Further details regarding the T_g determination methodology and validation with previous work have been included in Section S2 of the ESI.†

2.3 Simulations on moisture contaminated cells

The Amorphous Builder module in MAPS was employed to randomly inset 50 water molecules (simulating a moisture contamination of approximately 3.5% by wt) to the equilibrated crosslinked systems. Fig. 2(a) and (b) depict a dry crosslinked system and a moisture contaminated crosslinked system respectively. A blown-up view of one of the unreacted epoxy rings and a crosslinked site in a dry simulation cell is also provided in Fig. 2. After the water molecules were inserted, the 20% network was comprised of 3934 atoms and had simulation cell lengths of $x = y = z = 34.098$ Å. The 81% network was comprised of 3926 atoms with simulation cell lengths of $x = y = z = 34.328$ Å.

Epoxy resins generally absorb anywhere between 3–4% of moisture in the linear region of the absorption curve.[20] For every system with a particular crosslink density, three representative systems were created by randomly perturbing a fixed number of water molecules in the system. This resulted in 6 different simulation systems: 2 different crosslink densities and 3 representative systems for each crosslink density. The creation of multiple systems for a single crosslink density allowed us to take an average over three different systems and reduce the probability of an outlier.

Once moisture was introduced in the system, a 500-step geometry optimization was performed on each system using the Steepest Descent method as described previously. Post-optimization, the systems were subjected to a long *NPT* production run of 5 ns (5000 ps). It was imperative to allow sufficient time for the water molecules to navigate the entire polymer network. Hence, a long simulation time period was chosen to permit an accurate estimation of the hydrogen bonds formed by the polar molecules after proper equilibration.

The H–O bond length and the H–O–H bond angle was kept fixed using the 'fix-shake' command in LAMMPS because water molecules have a fixed bond length and bond angle of 0.96 Å and 104.5°, respectively.[65] Allowing the bond length or angles to vary during the simulation would produce unphysical results.

3. Results and discussion

3.1 Secondary bonding characteristics

3.1.1 Radial distribution function. The Radial Distribution Function (RDF) gives the probability of finding a particle at a

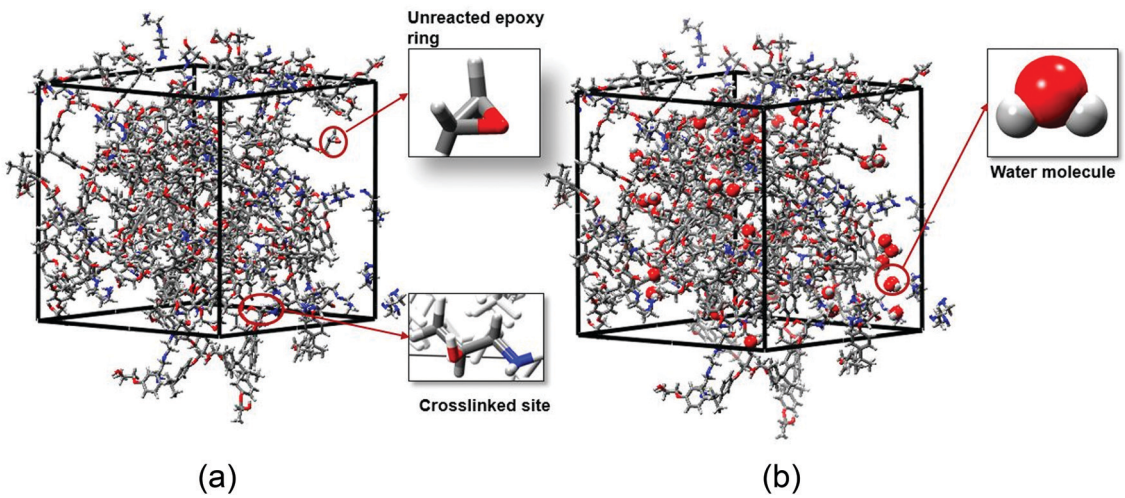

Fig. 2 (a) Simulation cell without moisture contamination. (b) moisture contaminated simulation cell.

distance "*r*" from a given reference particle.[66] A detailed explanation of RDF and its implications in an amorphous system is provided in Section S3.1 of the ESI.†

In the case of a moisture contaminated polymer network, the RDF plot is a useful qualitative tool for determining the probability of hydrogen-bonds between two polar species. The presence of peaks in the amorphous epoxy signifies higher probability of certain polar atomic species to be separated at a fixed distance. For an intermolecular RDF plot, the peaks within 3.5 Å are due to the hydrogen-bonds while the peaks beyond that are due to van der Waals and electrostatic interactions.[47,67,68] In this study, we calculated the RDF for two different sets of atomic species. First, we calculated the intermolecular RDF between the oxygen (Ow) and the hydrogen (Hw) atoms of the water molecules with increasing temperature and then proceeded to calculate the intermolecular RDF between the water molecules and the polar hydroxyl (–OH) sites in the network. The former set of calculations sheds light on how the water molecules interact with each other in the network as temperature increases while the latter set is critical in understanding the secondary bonding activity between the water molecules and one of the highly polar sites in the network. The calculations were done for both networks and an average value was calculated from the three representative systems at a given crosslinking density. This procedure was repeated at increasing temperatures and the results have been compiled in Fig. 3(a, b) and 4(a, b).

From a direct comparison of Fig. 3 and 4, we can conclude that the probability of an intermolecular H-bond between two water molecules is notably higher when compared to an H-bond between a water molecule and an –OH site. When we consider the intermolecular RDF of the water molecules (Fig. 3), we can see two clear peaks at ~1.9 Å and ~3.2 Å. It has been referenced in multiple studies[69–71] that these two peaks correspond to the Ow–Hw hydrogen bond between two water molecules with the second peak representing the second hydrogen atom of an H-bonded neighbor. If we compare the first peaks in Fig. 3(a) and (b), we can observe that a water molecule in the network with lower crosslinking density (20%) has a higher probability to form an H-bond at room temperature

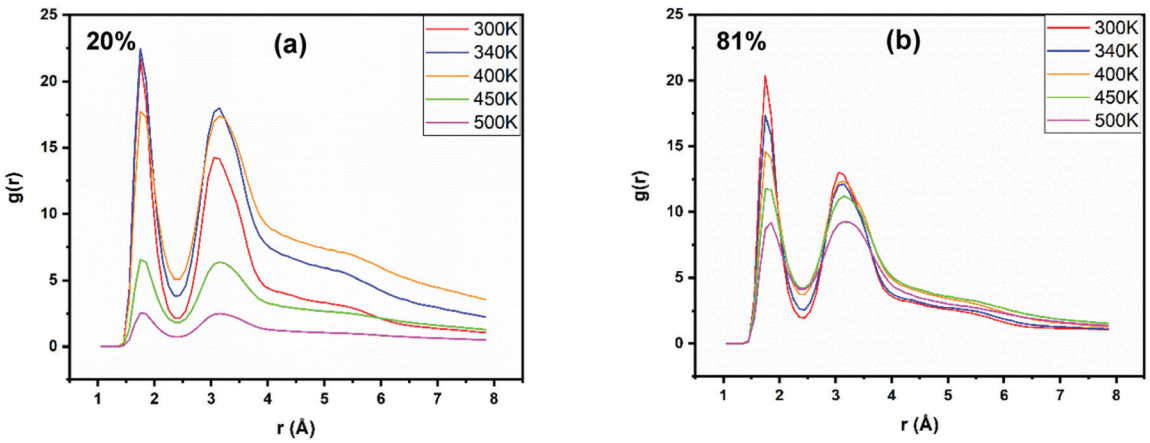

Fig. 3 Intermolecular RDF between water molecules for (a) 20% crosslinked network and (b) 80% crosslinked network.

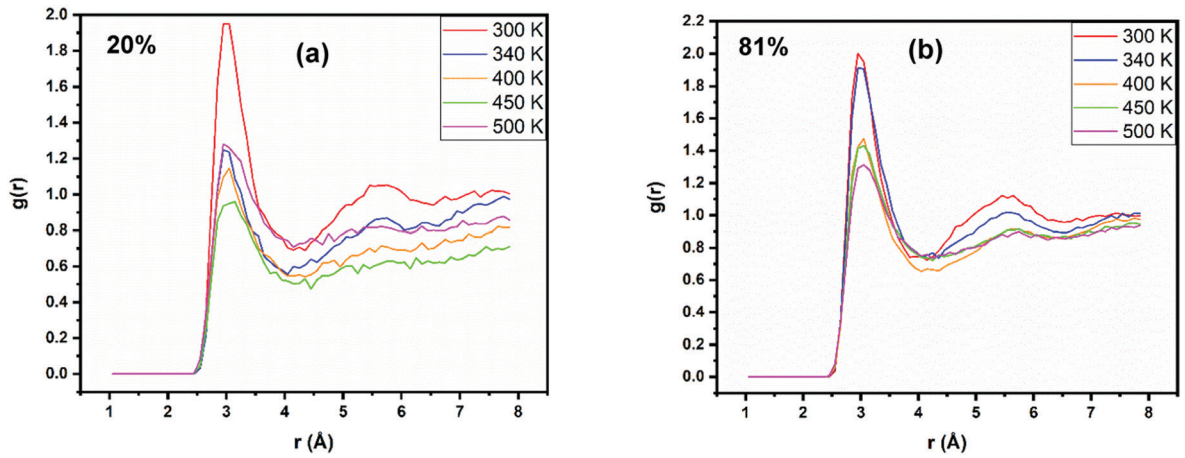

Fig. 4 Intermolecular RDF between the oxygen of the water molecules (Ow) and the polar oxygen of the hydroxyl group (OH) for (a) 20% crosslinked network and (b) 80% crosslinked network.

(300 K). This is a direct consequence of the lower polarity of the network and, as reported in previous studies,[40,58,72] indicates the higher probability of water molecules to form clusters in networks with lower crosslinking densities. As the temperature increases to 340 K, we observe that the H-bonding probability in the 81% crosslinked network decreases, but the H-bonding network is not disturbed in the 20% crosslinked network. We can infer from this observation that a slight rise in temperature is not enough to disturb the secondary bonding in the water clusters present in the network with lower crosslinking density. At higher temperatures beyond 340 K, the peak falls off for both networks, signifying a lower probability of mutual H-bonding between water molecules. The decrease in the H-bond formation probability beyond 373 K (400 K and beyond) is a direct consequence of the phase change of the water molecules.

In Fig. 4(a) and (b), the intermolecular RDF between the oxygen in the hydroxyl site and the oxygen in the water molecule (Ow) is compiled. We can observe a sharp peak at ~2.8 Å which corresponds to the H-bond between the water molecules and the polar oxygen atom at the hydroxyl site.[54,56] An intermolecular H-bond of this type between a water molecule and a network site represents the bound water in the epoxy.[24,26,27] For this type of H-bonding, we see that at room temperature, the 81% crosslinked network has a slightly higher probability of forming a bond when compared to the 20% crosslinked network. The higher crosslinking density generates more –OH sites, which increases the probability of a water molecule engaging in secondary bonding. As the temperature increases, the probability to form an H-bond decreases in both networks, but in the 20% crosslinked network the peak falls sharply when the temperature rises to 340 K. In contrast, there is a negligible dip in the peak for the 81% crosslinked network. An interesting conclusion about the H-bonding activity can be drawn from a simultaneous comparison of the results in Fig. 3 and 4. A significant rise in temperature is necessary to disturb the water clusters and break the intermolecular Ow–Hw hydrogen bonds in the lower polarity network. On the other hand, in the higher polarity network, the hydrogen bonds formed between the polar sites and the water molecules, constituting the ''bound'' water is considerably more stable under the influence of a rising temperatures. Similar trends are observed in the RDF plots calculated between Ow and the nitrogen (N) atoms present in the epoxy. These interactions, which are another form of a Type-II interaction, were weaker than the Ow–OH case. Additional detail about these RDF plots has been provided in Section S3.2 of the ESI.†

A peculiarity is observed in the lower polarity network (Fig. 4(a)) where we observe a higher peak at temperatures of 500 K. This can be interpreted as a rise in the intermolecular H-bonding activity, but an important point to consider here is that a temperature of 500 K is well beyond the glass transition temperature of any epoxy network,[13,16,73,74] especially one with a crosslinking density as low as 20%. As depicted in Fig. 5(a), at such high temperatures the short chain segments in this network will start flowing outwards and the polymer network will completely disintegrate. The movement of the chain segments is also evidenced in the exponential increase in available free volume (Fig. 12) in the 20% crosslinked network at higher temperatures. Therefore, the higher peak at 500 K should be considered an outlier.

3.1.2 H-Bonding activity. The state of water molecules and their mobility in an epoxy network is primarily dictated by the type of hydrogen bonds (H-bonds) formed by the molecules and their respective concentrations. As discussed earlier, an epoxy

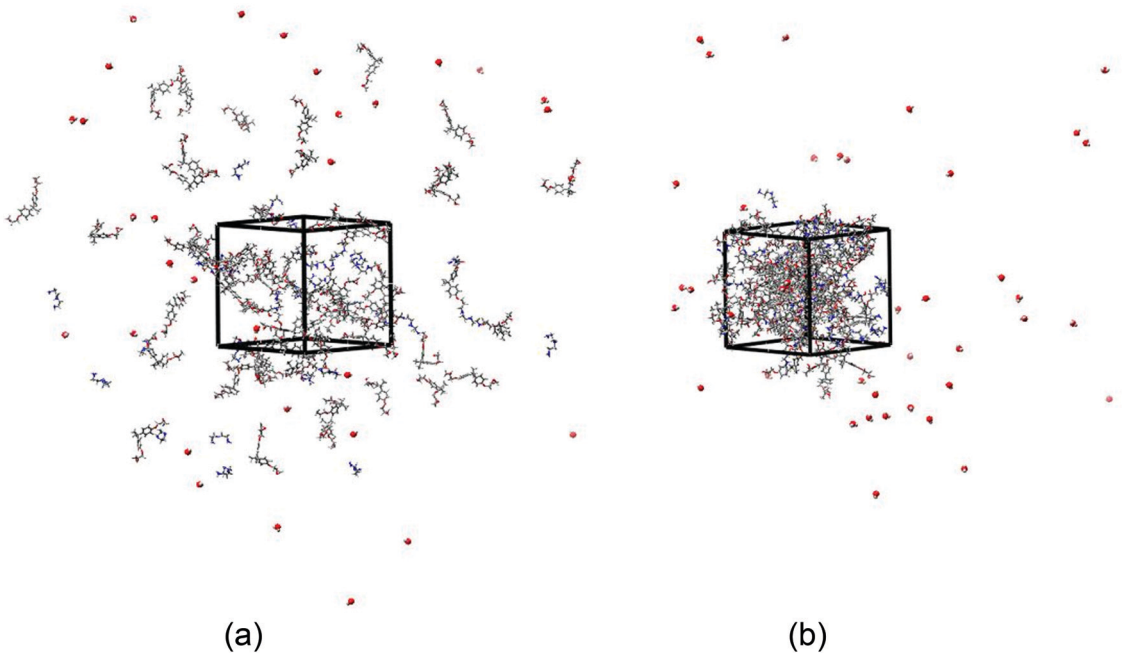

Fig. 5 (a) 20% crosslinked network at 500 K. (b) 81% crosslinked network at 500 K.

network has multiple polar sites which are partially charged due to the electronegativity differences between the participating atoms in a covalent bond of the network. Additionally, water itself is a highly polar molecule due to the large electronegativity difference between hydrogen and oxygen. Table S1 in the ESI† summarizes the different polar species in the epoxy–water system of our study and the respective partial charges assigned to them. All of the polar species that have a partial negative charge are potential acceptors, while the hydrogen atoms with a partial positive charge are donors. In our study, the H-bond was calculated based on a geometric criterion, *i.e.* if the distance and the angle between a donor–acceptor pair was found to be below a certain threshold, then it was assumed that a H-bond was present at that site. We used a Python script in MAPS for counting the number of H-bonds with a cut-off distance of 2.5 Å and a cut-off angle of 90°.[58] For a selected group of atoms, the H-bonds were counted over the entire simulation period of 5 ns (5000 ps) and then an average value was calculated over the last 1 ns of the simulation time frame. This was done to ensure that the H-bond values are calculated only after the system has been well equilibrated. Similar to the RDF, this procedure was repeated for all the three simulated systems created at a particular crosslink density and the average value at different temperatures was considered for further analysis. The error bars at any observation point are due to the standard deviation from the three systems at each crosslinking density.

The two polymer networks considered in this study are very similar apart from their crosslinking density; they have the same chemical constituents and are contaminated with the same amount of moisture (by wt%). Therefore, it is worthwhile to analyze the total number of H-bonds formed by the networks at the different temperatures to understand how the variation in crosslinking density manifests itself in the overall secondary bonding characteristics. This was done by including all the polar species listed in Table S1 (ESI†). The results are illustrated in Fig. 6. The carbon atoms in the network had negligible charge ($<\pm0.1$) and were considered non-polar. The results in the figure are the collection of three different types of H-bonds:

(i) The H-bonds formed by the polar sites in the network among themselves due to the crosslinked network structure.

(ii) The H-bonds formed between the water molecules dispersed in the network.

(iii) The H-bonds formed between the water molecules and the polar sites.

From the figure, two conclusions are evident: (1) the total number of H-bonds in both networks decrease with increasing temperature, and (2) the network with higher crosslinking (81%) consistently forms a greater number of H-bonds when compared to the other network (20%). The decrease in H-bonding with temperature is a direct consequence of the greater amount of energy available in the network, which allows the polar sites to easily break secondary bonds through thermal excitation while the greater availability of highly polar-OH sites in the 81% crosslinked network results in the enhanced overall H-bonding activity.

Consequently, the three possible types of H-bonds that can be formed by the networks were studied in greater detail. Fig. 7 demonstrates the temperature variation in the number of H-bonds formed by the polar sites in both networks. As expected, we observe a linear downward trend with increasing temperature and the polar sites in the highly crosslinked network are consistently involved in a greater number of H-bonds owing to its higher polarity. The more compelling inferences are drawn when we observe the H-bonding activity of the water molecules in the network. As noted earlier, if two water molecules form a mutual H-bond between themselves, then the oxygen atom of one water molecule (Ow) will act as an acceptor while the hydrogen atom of another water molecule will be the donor (Hw). These types of H-bonds have been denoted as Type-I in this study, while the H-bonds formed by the water molecules with the polar sites have been denoted as Type-II. The nomenclature used is consistent with our previous studies.[34,40]

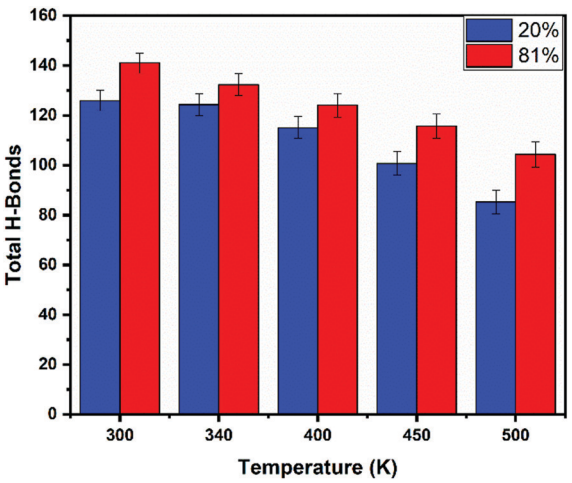

Fig. 6 Total H-bonds formed by all polar species at different temperatures.

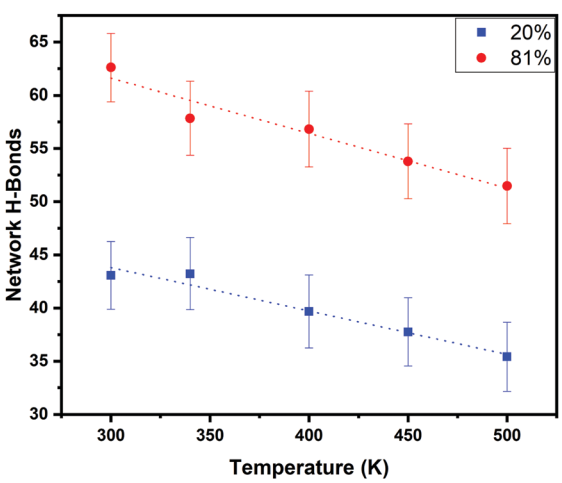

Fig. 7 Temperature variation in the H-bonds formed by the polar sites in the network.

For calculating the exact number of Type-II H-bonds, the Type-I H-bonds and the H-bonds formed by the network (Fig. 7) were subtracted from the total number of H-bonds (Fig. 6). The temperature variation of the Type-I and II H-bonds in both networks have been depicted in Fig. 8(a) and (b) respectively. The results have been normalized per water molecule in the respective polymer networks to clearly convey the tendency of a water molecule to form a specific type of H-bond *versus* another type.

The first detail we can observe from Fig. 8 is that, in both networks, the number of Type-I H-bonds is always higher than the Type-II H-bonds irrespective of the temperature. This indicates that water molecules have a much higher probability of forming an H-bond with another water molecule compared to a network polar site. As mentioned in the previous section, the magnitude of the Type-II H-bonds is a direct indicator of the water molecules "bound" to the polymer network. The concentration of these bonds is always lesser in a polymeric network when compared to the free water (Type-I H-bond), as revealed in previous experimental[29,30] and simulation[40,56] studies. The results are also consistent with the RDF plots of the previous section which depicted that the peaks for the intermolecular Ow–Hw H-bonds were considerably higher (Fig. 3) when compared to the RDF between the water molecules and the polar sites (Fig. 4). We also observe that initially the network with lower polarity (20%) has a greater magnitude of Type-I H-bonds (free water) when compared to the highly crosslinked network (81%). Conversely, the 81% crosslinked network reveals slightly higher initial concentration of Type-II H-bonds with respect to the 20% crosslinked network. These observations are also consistent with the peak magnitudes of the RDF plots at room temperature and are a direct consequence of the difference in the available polar sites. If we look at the trends with increasing temperature for both networks, we see one important distinction. The network with higher crosslinking (Fig. 8(b)) uniformly demonstrates a linear downward trend with temperature for both the Type-I and Type-II H-bonds. But, for the 20% crosslinked network, the concentration of Type-I H-bonds is nearly constant with an initial increase in temperature followed by a downward trend at higher temperatures. The Type-II H-bonds decrease initially and then reveal slightly elevated H-bond concentrations at the higher temperatures.

The most interesting takeaway from these trends is that although they are quantified based on a geometric criterion, they have similarities with the qualitative trend of the RDF plots in the previous section. As illustrated in Fig. 3(b) and 4(b), the peaks for both the RDF plots in the 81% crosslinked network degrade linearly, which mirrors the Type-I and II H-bond concentration trends in Fig. 8(b). On the other hand, we see that the Ow–Hw RDF peak (Fig. 3(a)) is not disturbed as the temperature increases from 300 K to 340 K in the 20% crosslinked network, which then degrades with increasing temperature while the Ow–OH RDF peak (Fig. 3(b)) initially falls off before depicting a slightly higher peak at 500 K. This bears a strong correlation with the trends observed in Fig. 8(a). The water molecules in the 20% crosslinked network have a greater tendency to cluster together[40,58,72] and the Ow–Hw H-bonds formed in these clusters are only disturbed with a significant increase in temperature. As discussed earlier, the rise in the Type-II H-bonds at 500 K should be considered an outlier since the network, owing to the combined effects of low crosslinking and extremely high temperature, is completely disintegrated at this point (Fig. 5(a)).

3.1.3 Dynamic behavior of H-bond (autocorrelation function). In the previous section, the secondary bonding phenomenon was quantified through the average number of hydrogen bonds formed during the simulation period. The dynamic behavior of these secondary bonding interactions was not investigated. The average lifetime of the individual hydrogen bonds can reveal important information about the strength of these interactions as water molecules break and reform H-bonds while navigating the network during the simulation.

To investigate the dynamic behavior of the H-bonds, the Autocorrelation Function (ACF), given by $C(t)$, was calculated by

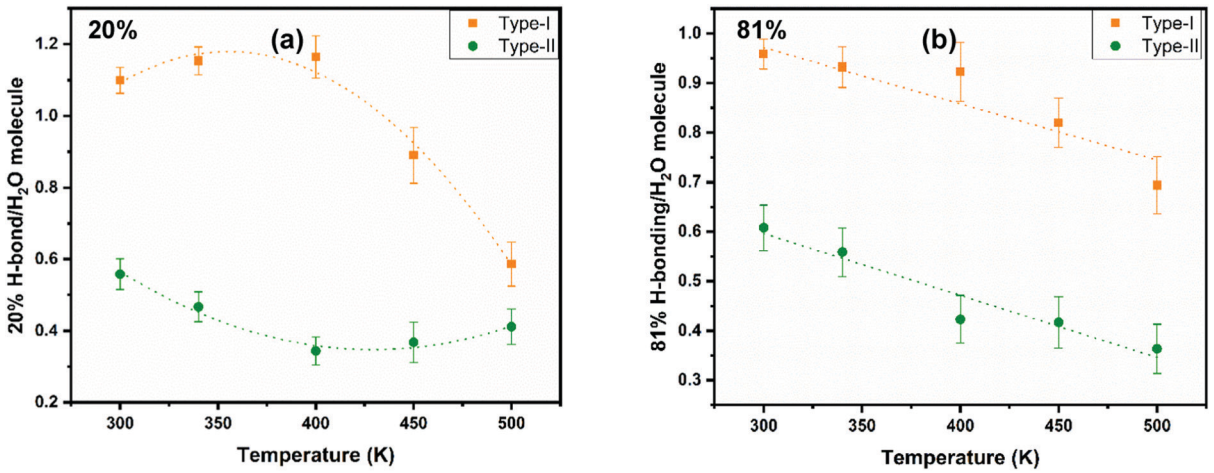

Fig. 8 Temperature variation in the different type of H-bonds formed per molecule of water in (a) 20% crosslinked and (b) 81% crosslinked network. Values are normalized per water molecule.

monitoring the hydrogen bonds formed by a tagged pair during the simulation trajectory as seen in eqn (1):[75]

$$C(t) = \frac{\langle h(0)h(t)\rangle}{\langle h^2\rangle} \quad (1)$$

where $h(t)$ is a binary function for each H-bond pair between a donor and acceptor group of interest. $h(t)$ takes a value of 1 if the group is bonded at time t and 0 otherwise. The definition of the lifetime of an H-bond can be defined as either continuous ($C_c(t)$) or intermittent ($C_I(t)$). In case of $C_c(t)$, the time during which a particular H-bond remains continuously attached is considered. In the case of $C_I(t)$, an H-bond can break, subsequently reform, and be counted again.[76]

In this work, two different types of $C_I(t)$ were calculated as a function of increasing temperatures for both networks. For the first case, the lifetime of an H-bond between two water molecules in the network was monitored. In the latter, the dynamics of the H-bond formed between a water molecule and the polar hydroxyl sites was studied. The trends of the $C_I(t)$ curves can qualitatively portray the relative dynamic behavior of H-bonds with the different polar sites, but they fail to quantify the average lifetime of these bonds. To solve this issue, the calculated ACFs were fitted to the two-parameter exponential Kohlrausch–Williams–Watts (KWW)[56,75] form:

$$C_I(t) = \exp\left[-\left(\frac{t}{\tau}\right)^{\beta}\right] \quad (2)$$

where τ and β denote the relaxation time and the stretching exponent, respectively. The magnitude of τ gives an estimate of the average time it takes for the water molecules to form and subsequently break a particular type of H-bond. The KWW fit of the $C_I(t)$ for both the cases have been compiled in Fig. 9 and 10.

From the figures, we can clearly conclude that for both cases, the decay in the correlation function becomes more rapid as the temperature increases. In the 20% network, the decay is steep in both the water–water and water–hydroxyl case as soon as the temperature increases to 340 K while the decay is comparatively gradual in the 81% network. We suspect that the steep decay in the 20% network is due to the lower T_g. The better structural integrity of the 81% network leads to a higher

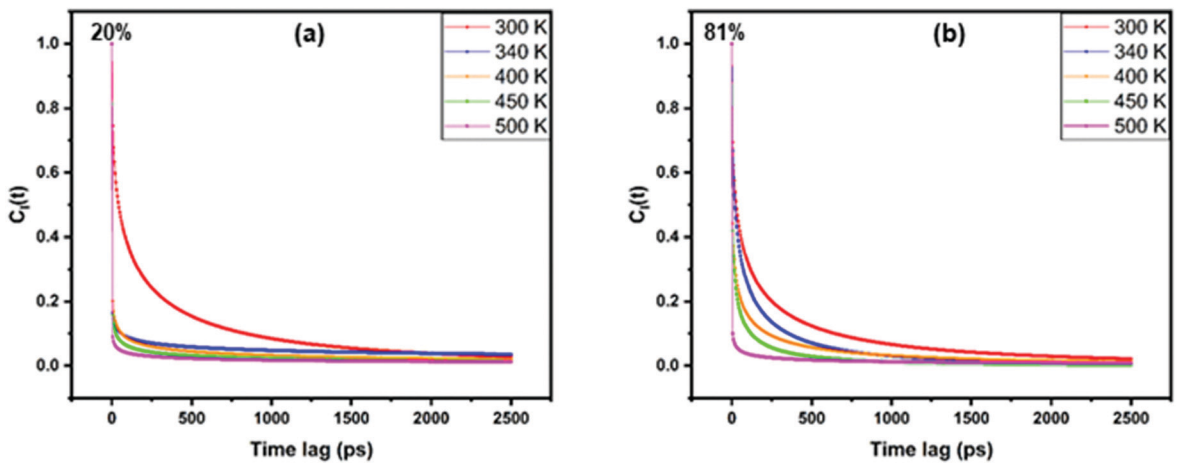

Fig. 9 Temperature variation of the water–water H-bond ACF (KWW fit) in the (a) 20% crosslinked and (b) 81% crosslinked network.

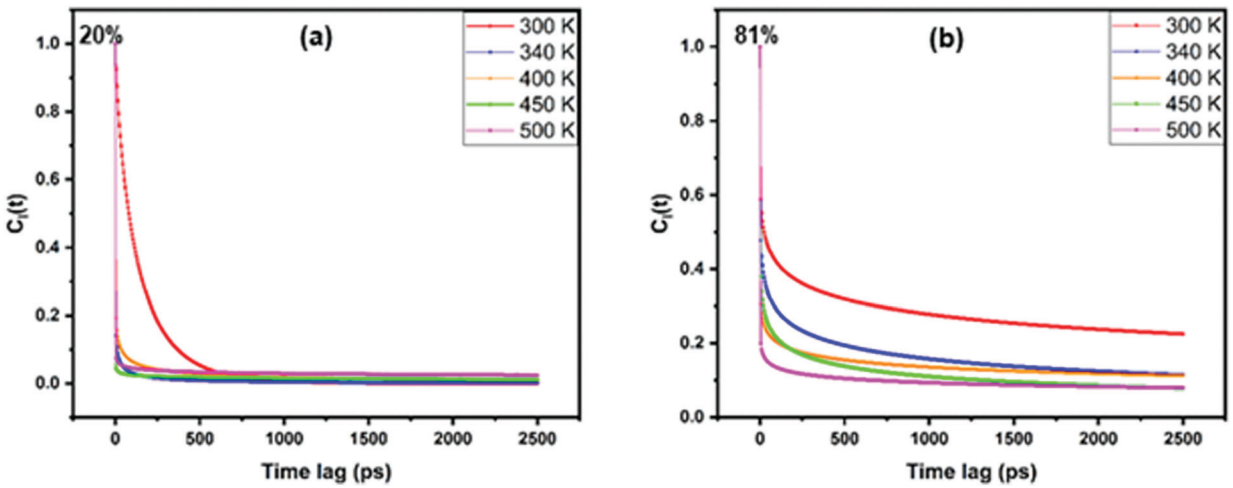

Fig. 10 Temperature variation of the water–hydroxyl H-bond ACF (KWW fit) in the (a) 20% crosslinked and (b) 81% crosslinked network.

T_g which in turn leads to greater stability of individual H-bonds even at higher temperatures.

The magnitude of τ obtained from the exponential fit for both the networks and the two different H-bonding cases has been compiled in Table 1. A uniform designation is given to all the calculated values of τ which is below the trajectory output time period of 5 ps.

The data in the table suggests that the H-bonds are most stable at 300 K. As the temperatures in both networks exceeds the T_g, the lifetime of individual H-bonds becomes increasingly transient. We also observe that the water–water H-bond at 300 K is more stable in the 20% network while the lifetime of the water–hydroxyl bonds has greater stability in the 81% network. These takeaways are consistent with the results of our previous sections, which have shown that the water molecules tend to cluster in the 20% crosslinked network and have a higher tendency to engage in a hydrogen bond with the network when the crosslinking density increases.

3.2 Diffusivity and activation energy

3.2.1 Mean squared displacement (MSD) and diffusion coefficient. The diffusion coefficient (D) of the water molecules at different temperatures provides an estimate of the mobility of moisture in the individual networks.[51] In MD simulations, D can be calculated from the mean square displacement (MSD) curves of the water molecules during the simulation time period. The MSD of thermally excited water molecules can be defined as its trajectory with time as it randomly traverses the polymer matrix[49] and is given by eqn (3):

$$\mathrm{MSD}(t - t_0) = \frac{1}{6N}\sum_{i=1}^{N}(r_i(t) - r_i(t_0))^2 \qquad (3)$$

where $r_i(t)$ is the position of the center of mass of the ith water molecule at time t. The diffusion coefficient can be estimated from the MSD curve by finding the slope in the initial linear region[51,77] as shown in eqn (4):

$$D = \lim_{t\to\infty}\frac{\mathrm{d}}{\mathrm{d}t}\mathrm{MSD}(t - t_0) \approx \left\langle \frac{\mathrm{d}}{\mathrm{d}t}\mathrm{MSD}(t - t_0)\right\rangle_{t_1}^{t_2} \qquad (4)$$

The initial part of the MSD curves is generally neglected because these regions are mostly non-linear. Fig. S5 in ESI† illustrates the MSD curves for the water molecules at different temperatures and the simulation time period chosen to apply eqn (2).

The temperature variation in the diffusion coefficient in the two networks was then investigated and the results have been illustrated in Fig. 11. Similar to the previous results, each data point in the plot is an average of three models and the error bars signify the standard deviation in the calculated diffusion coefficient at a particular temperature.

From the results compiled in Fig. 11, we can observe that, irrespective of the temperature, the diffusion coefficient in the highly crosslinked network is consistently lower than the other network. This deviation increases remarkably at higher temperatures. It is safe to assume that at lower temperatures the suppressed diffusivity in the 81% crosslinked network is an artefact of the enhanced H-bonding with the network which leads to a greater fraction of water molecules being "bound" to the network and as a direct consequence, impedes its mobility. At higher temperatures, beyond 400 K, we are above the glass-transition temperature (T_g)[13,16,73,74] of the polymer networks and as discussed in the previous section (Section 3.1.1), this will result in the uncrosslinked chain segments in the 20% crosslinked network to slide and move outwards and a significantly greater amount of free volume will be generated. There will be a rise in free volume even in the 81% crosslinked network, but this will be lower since the chains will be held together due to the higher crosslinking density (Fig. 5(b)). This can be clearly observed in Fig. 12, where the variation in available free volume has been plotted with increasing temperatures for both networks. Initially, both networks have similar free volume. However, as the temperatures increase, the difference in free volume in both networks increases manifold. This combined effect of lower H-bonding with the network and a greater availability of free volume results in the notable differences in diffusion coefficient (D) at higher temperatures.

Water activation energy at different temperatures. During the desorption process of moisture from epoxies, a certain fraction

Table 1 Magnitude of relaxation time (τ) for the different types of H-bond in both networks

% crosslinking	Temperature/K	τ (water–water H-bond)/ps	τ (water–hydroxyl H-bond)/ps
20	300	21.1	25.6
	340	<5	<5
	400	<5	<5
	450	<5	<5
	500	<5	<5
81	300	14.4	45.4
	340	9.2	5.8
	400	<5	<5
	450	<5	<5
	500	<5	<5

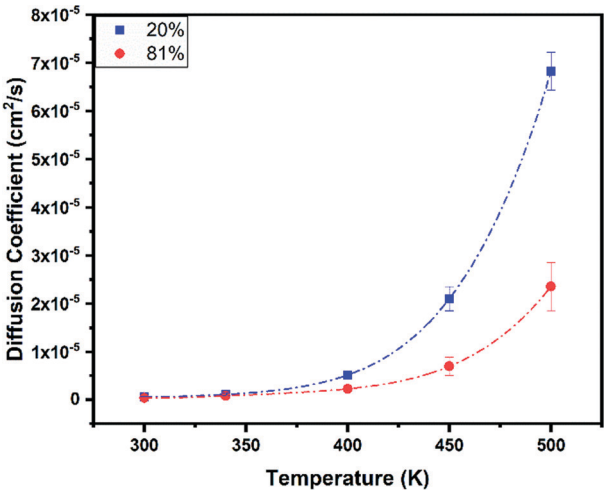

Fig. 11 Diffusion coefficient as a function of temperature for both the polymeric networks.

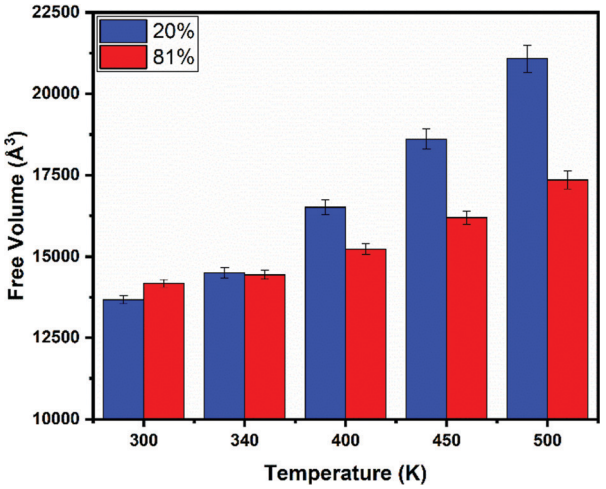

Fig. 12 Available free volume as a function of temperature for both polymeric networks.

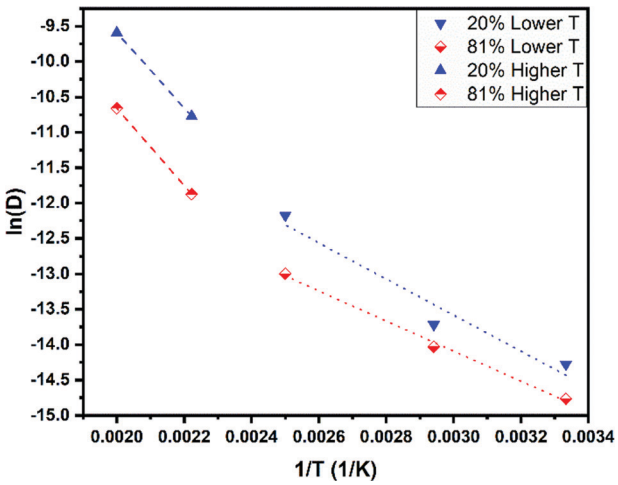

Fig. 13 Graph to calculate activation energy of water from difference of slope in $1/T$ *vs.* $\ln(D)$.

of residual water is always present in the system irrespective of the desorption time frame. To explain this phenomenon, Zhou *et al.*,[60] postulated the existence of two types of bound water. The tightly bound Type-II water molecules have a higher activation energy and consequently a higher desorption temperature.[19,60] The activation energy of the water molecules involved in the diffusion process is dependent on the energy barriers that the molecules have to overcome due to the interaction potential from intramolecular forces.[6,78] The substantially higher number of polar sites in the 81% crosslinked network will create an enhance interaction potential for the water molecules and hence a greater activation energy in the highly crosslinked network.[78]

The Arrhenius equation, given by eqn (5), relates the diffusion coefficient of any penetrant molecule at different temperatures, and is given in the log form in eqn (6), where Q is the activation energy of the different species of water molecules.

$$D = D_0 \exp\left(-\frac{Q}{RT}\right) \tag{5}$$

$$\ln(D) = \ln(D_0) - \frac{Q}{RT} \tag{6}$$

Fig. 13 is a plot of $1/T$ *vs.* $\ln(D)$ and for a particular network, we observe that the slope at lower temperatures is different than the slope at higher temperatures. This bolsters the idea of the existence of tightly bound water molecules that have a higher activation energy. The difference in activation energies was calculated from the difference in slope for both networks and are given in Table 2.

The results from our simulations illustrate that the energy required to desorb all of the water molecules is $\sim$11 kcal mol^{-1} ($\sim$46.024 kJ mol^{-1}), which is in excellent agreement with previous experimental[28,35,36,79,80] and simulation studies.[51] The energy required for breaking a hydrogen bond ranges between 5 and 20 kcal mol^{-1}.[60,81] We observe that the difference in activation energies of the two species of water is in this range, which suggests that the tightly bound water molecules are involved in H-bonding with the polymer network and, hence, require a greater activation energy to desorb out of the network. The difference in activation energies for the two water species is higher in the 81% crosslinked network by approximately 21%, which reaffirms the fact that the H-bonding activity between water and the polymer network is higher at higher crosslinking densities. In the case of in-service composites, the polymer matrix always has a very high crosslinking density that imparts better mechanical performance. Hence, they will presumably always have a higher fraction of residual moisture that will be difficult to completely eradicate from the network.

3.3 Dielectric activity

3.3.1 Dielectric signature of water. MD simulations can be used to obtain the dipole moment fluctuations (M) of a group of atoms during the simulation trajectory. These fluctuations reveal critical information regarding the dielectric activity and ultimately the static dielectric constant of the system. The static permittivity of different water models (SPC/E, TIP3P) has already been extensively studied[82–87] and different relations have been formulated depending on how the long range electrostatic interactions are computed in the simulation.

In our case, the particle–particle particle-mesh (PPPM) method is used for the long-range electrostatics which is a modification of the Ewald summation method.[88] Several of the aforementioned studies that have employed the Ewald summation[85–87] used eqn (7) to calculate the dielectric constant of water

$$\varepsilon - 1 = \frac{\langle M^2 \rangle}{3kTV} \tag{7}$$

where M is the total dipole moment of the water molecules, k is the Boltzmann constant, T is the temperature and V is the volume. In our study, we used eqn (7) for the calculation of the dielectric constant. The dipole moment fluctuations (M) of the water molecules in both systems at different temperatures

Table 2 Calculation of the difference in activation energy for the tightly bound water molecules

Cross-linking	Lower temp. slope ($-Q/R$)	Lower temp. activation energy (kcal mol^{-1})	Higher temp. slope ($-Q/R$)	Higher temp. activation energy (kcal mol^{-1})	Difference in slope	Difference in activation energy (kcal mol^{-1})
20%	−2548.05	5.06	−5302.85	10.54	−2754.80	5.5
81%	−2128.75	4.23	−5467.08	10.86	−3338.33	6.6

were evaluated over the simulation time period of 5 ns using the MAPS analyzer and an average dipole moment ($\langle M \rangle$) was calculated. M is given by:

$$M = \sum_i \mu_i \quad (8)$$

where μ_i is the dipole moment of molecule i (water in our case).

As discussed in our previous study,[40] the water molecules that are bound at the polar sites will have restricted dipolar rotations due to secondary interactions with the network. These water molecules will have a lower dipole moment compared to the free water in the network. Therefore, if the moisture contamination (by wt%) is held constant, the average dipole moment should be lower in the system which has a greater fraction of bound water molecules. This is what we observe in Fig. 14 at room temperatures (300 K) where the 81% cross-linked network has a notably lower average dipole moment when compared to the 20% network. But as soon as the temperature increases, the fluctuations in both networks become very similar. If we only go by the trends in Fig. 14, we might conclude that the significant difference in crosslinking density will not affect the dielectric constant when the networks are subjected to higher temperatures, but a closer look at eqn (7) reveals that the dielectric constant (ε) is not dependent solely on the average dipole moment. It is also influenced by the available free volume for the water molecules and the temperature, both of which are increasing. Fig. 15 provides the dielectric constant that is calculated by plugging in the values for the average free volume (Fig. 12) and the temperature in eqn (7).

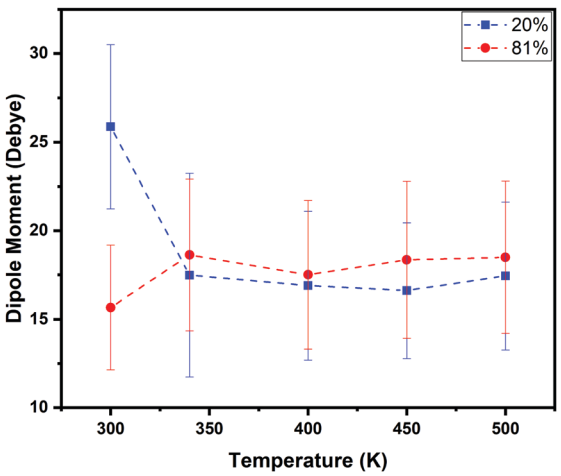

Fig. 14 Average dipole moment fluctuations of the water molecules as a function of temperature.

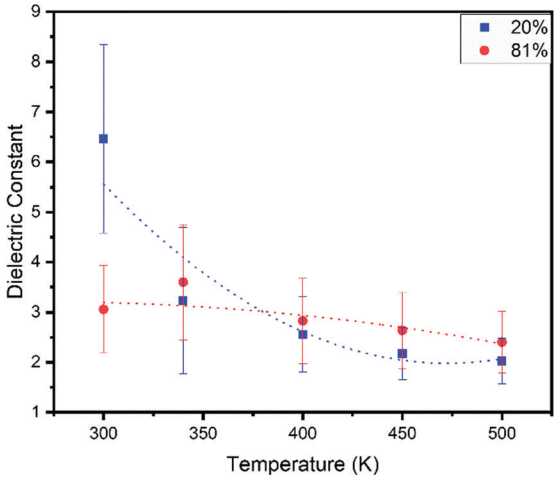

Fig. 15 Dielectric constant of the water molecules in the two networks as a function of temperature.

The dielectric constant of bound water has been assumed to be similar to that of ice, having a magnitude of ~3.2.[2,89] The dielectric constant of free water at room temperature (298.14 K) is much higher (~80) across a wide range of frequencies (1.3–40 000 MHz).[90] In our study, we have a mixture of free and bound water which is dispersed within the network and the overall moisture concentration is relatively low (3.5 wt%). Due to the largely constrained nature of water within a polymer network, it is expected that the effective dielectric constant of the absorbed water molecules will be very different from bulk water (ε = 80). The observed value between 3 and 7 for the two networks at 300 K is reasonable. We observe a decreasing trend in both networks, but the dielectric constant in the 20% cross-linked network degrades very quickly. The average magnitude of the dielectric constant falls from 6.5 to 2.0 corresponding to a degradation of ~70%. This is a result of this network having a higher concentration of "free" water existing in the water clusters that will contribute to an elevated dielectric activity, but this will quickly drop off with increasing temperature. As observed in the previous sections, the free water molecules do not engage in extensive secondary bonding with the network and hence have a lower activation energy for desorption. Therefore, as the temperatures increase, these water molecules quickly diffuse out of the network and, consequently, the dielectric constant decreases. For the network with higher crosslinking density, the dielectric constant is initially lower when compared to the 20% network and we observe a very slight downward trend. The magnitude of the dielectric constant holds up across the wide temperature range and we see a degradation of ~20%. This indicates that the greater fraction of bound water will

result in suppressed dielectric activity, which could be beneficial for a highly crosslinked composite matrix being used in radome structures. However, if the moisture contamination is high and the concentration of bound water increases in the matrix, the higher activation energy for these molecules will ensure that the dielectric constant will not decrease even if the composite is subjected to high temperatures.

The range of temperature variations of the dielectric constant is well within the range of the experimental setup in our previous study which can detect changes in dielectric constant on the order of 10^{-3}.[18]

4. Conclusions

An accurate understanding of the distribution of the state of water molecules in an epoxy network is a challenging task due to the large number of influencing factors. The behavior of water in a polymer network is poorly understood and is likely to remain a topic of active research as the overall utilization and longevity of polymer matrix composites continues to increase. In this work, an epoxy network was studied over a wide range of temperatures to better understand how changes in polarity and network structure can influence the nature of secondary interactions even when the chemical constituents and the concentration of moisture is held constant. The results suggest that polarity influences the type of secondary interaction activity of water molecules within the polymer network. Although both Type-I and Type-II interactions decrease with a greater availability of thermal energy, the Type-I H-bonds potentially present in the water clusters of the lower polarity network are stronger when compared to the other network with higher polarity. Conversely, this higher polarity demonstrates preferential formation of Type-II H-bonds due to the increased availability of highly polar hydroxyl sites. These phenomenological differences in the secondary bonding activity have a direct impact on the diffusion of water molecules as the temperature increases. We observed that desorption activation energy for the tightly bound water molecules is higher by approximately 20% (6.6 kcal mol^{-1} compared to 5.5 kcal mol^{-1}) in the highly crosslinked matrix. This was attributed to the fact that water molecules need increased energy to be mobilized when they are involved in extensive secondary bonding with the network. The dielectric activity was also affected by these interactions as the dielectric constant of the water molecules decreased by $\sim$70% in the 20% crosslinked network, where the activation energy was lower. The decrease was much more subtle in the 81% crosslinked network ($\sim$20%).

These results are critical when studying the behavior of highly crosslinked matrices in a commercially available composite, particularly when the lifespan of the material is on the order of years. The ubiquity of atmospheric water virtually guarantees some level of moisture-driven degradation in these systems. This study highlights the difficulty of completely removing water molecules once a highly crosslinked epoxy network is contaminated with moisture. The findings also indicate that the dielectric activity is relatively immune to an increase in temperature when the polarity is high. Hence, it may be advisable to use highly polar networks in some scenarios where high electrical transmissivity is a critical performance factor, such as radomes.

The study is also supportive of prior indications of the potential for using absorbed water molecules as an imaging agent to detect damage in polymers. In the 20% crosslinked network, clustering was observed to drive up the dielectric constant of the water molecules. Therefore, in the presence of damage-induced micro cracks and voids, absorbed moisture can form clusters and result in locally higher dielectric constant in the damaged area. This difference in dielectric signature near the damage site may be useful in the design of novel non-destructive detection techniques using near infra-red spectroscopy and dielectric resonance techniques.

Author contributions

Rishabh Debraj Guha: conceptualization, methodology, software, data curation, visualization, writing – original draft. Ogheneovo Idolor: conceptualization, writing – review & editing. Katherine Berkowitz: visualization, writing – review & editing. Melissa Pasquinelli: methodology, data curation, visualization, writing – review & editing. Landon R Grace: supervision, project administration, funding acquisition, writing – review & editing.

Conflicts of interest

The authors declare that they have no known competing financial interests or personal relationships that could have appeared to influence the work reported in this paper.

Acknowledgements

The authors would like to acknowledge the support and insight of Dr Andrew Petersen (Advanced Computing, Office of Information Technology, NCSU) and the HPC cluster at NCSU for allotting us the computational time for running our simulations.

References

1 F. R. Jones and J. P. Foreman, *Polymer Composites in the Aerospace Industry*, Elsevier, 2015, pp. 335–369.
2 L. R. Grace, *Compos. Struct.*, 2015, **128**, 305–312.
3 Reports and Data. 2019. Composites Market To Reach USD 146.14 Billion By 2026.
4 F. Ellyin and C. Rohrbacher, *J. Reinf. Plast. Compos.*, 2003, **22**, 615–636.
5 B. Dębska and L. Lichołai, *Period. Polytech., Civ. Eng.*, 2016, **60**, 281–287.
6 J. Seo, W. Jang and H. Han, *Macromol. Res.*, 2007, **15**, 10–16.
7 C. L. Soles and A. F. Yee, *J. Polym. Sci., Part B: Polym. Phys.*, 2000, **38**, 792–802.
8 C. L. Schutte, *Mater. Sci. Eng., R*, 1994, **13**, 265–323.

9 O. Idolor, R. Guha and L. Grace, American Society for Composites 2018. A dielectric resonant cavity method for monitoring of damage progression in moisture-contaminated composites.
10 K. Berkowitz, O. Idolor and M. Pankow *et al.* SAMPE Long Beach 2018 Conference and Exhibition. Combined effects of impact damage and moisture exposure on composite radome dielectric properties.
11 H. N. Dhakal and Z. Zhang, *Wiley encyclopedia of composites*, 2011, pp. 1–7.
12 P. S. Theocaris, E. A. Kontou and G. C. Papanicolaou, *Colloid Polym. Sci.*, 1983, **261**, 394–403.
13 T. S. Ellis and F. E. Karasz, *Polymer*, 1984, **25**, 664–669.
14 L. R. Grace and M. C. Altan, *Composites, Part A*, 2012, **43**, 1187–1196.
15 L. R. Grace and M. C. Altan, *Polym. Compos.*, 2013, **34**, 1144–1157.
16 J. B. Enns and J. K. Gillham, *J. Appl. Polym. Sci.*, 1983, **28**, 2831–2846.
17 M. K. Bhuyan, M. S. Bhuyan and J. I. Rodríguez-Dévora, *et al.*, *J. Compos. Mater.*, 2013, **47**, 3421–3432.
18 O. Idolor, R. Guha and L. Bilich, *et al.*, American Society for Composites. 2019, 2-Dimensional Mapping of Damage in Moisture Contaminated Polymer Composites Using Dielectric Properties.
19 P. Moy and F. E. Karasz, *Polym. Eng. Sci.*, 1980, **20**, 315–319.
20 M. J. Adamson, *J. Mater. Sci.*, 1980, **15**, 1736–1745.
21 A. Apicella, R. Tessieri and C. de Cataldis, *J. Membr. Sci.*, 1984, **18**, 211–225.
22 L. W. Jelinski, J. J. Dumais and A. L. Cholli, *et al.*, *Macromolecules*, 1985, **18**, 1091–1095.
23 R. A. Pethrick, E. A. Hollins and I. McEwan, *et al.*, *Macromolecules*, 1996, **29**, 5208–5214.
24 C. Grave, I. McEwan and R. A. Pethrick, *J. Appl. Polym. Sci.*, 1998, **69**, 2369–2376.
25 D. Hayward, E. Hollins and P. Johncock, *et al.*, *Polymer*, 1997, **38**, 1151–1168.
26 A. Herrera-Gómez, G. Velázquez-Cruz and M. O. Martín-Polo, *J. Appl. Phys.*, 2001, **89**, 5431–5437.
27 S. Cotugno, G. Mensitieri and P. Musto, *et al.*, *Macromolecules*, 2005, **38**, 801–811.
28 P. Musto, L. Mascia and G. Ragosta, *et al.*, *Polymer*, 2000, **41**, 565–574.
29 P. Musto, G. Ragosta and L. Mascia, *Chem. Mater.*, 2000, **12**, 1331–1341.
30 P. Musto, G. Ragosta and G. Scarinzi, *et al.*, *J. Polym. Sci., Part B: Polym. Phys.*, 2002, **40**, 922–938.
31 S. Cotugno, D. Larobina and G. Mensitieri, *et al.*, *Polymer*, 2001, **42**, 6431–6438.
32 O. Idolor, R. D. Guha and K. Berkowitz, *et al.*, *Composites, Part B*, 2021, **211**, 108637.
33 O. Idolor, R. D. Guha and K. Berkowitz, *et al.*, Proceedings of the American Society for Composites—Thirty-Fifth Technical Conference, 2020, DOI: 10.12783/asc35/34874. Damage Detection in Polymer Matrix Composites by Analysis of Polymer–Water Interactions using Near-Infrared Spectroscopy.
34 R. D. Guha, O. Idolor and L. Grace, American Society for Composites, 2019, Molecular Dynamics (MD) Simulation of a Polymer Composite Matrix with Varying Degree of Moisture: Investigation of Secondary Bonding Interactions.
35 S. Li, L. Li and Y. Yu, *et al.*, *Corros. Sci.*, 2009, **51**, 3000–3006.
36 J. Mijović and H. Zhang, *Macromolecules*, 2003, **36**, 1279–1288.
37 C. L. Soles, F. T. Chang and D. W. Gidley, *et al.*, *J. Polym. Sci., Part B: Polym. Phys.*, 2000, **38**, 776–791.
38 C. L. Soles, F. T. Chang and B. A. Bolan, *et al.*, *J. Polym. Sci., Part B: Polym. Phys.*, 1998, **36**, 3035–3048.
39 K. Frank, C. Childers and D. Dutta, *et al.*, *Polymer*, 2013, **54**, 403–410.
40 R. D. Guha, O. Idolor and L. Grace, *Comput. Mater. Sci.*, 2020, **179**, 109683.
41 I. Yarovsky and E. Evans, *Polymer*, 2002, **43**, 963–969.
42 C. Wu and W. Xu, *Polymer*, 2006, **47**, 6004–6009.
43 V. Varshney, S. S. Patnaik and A. K. Roy, *et al.*, *Macromolecules*, 2008, **41**, 6837–6842.
44 C. Li and A. Strachan, *Polymer*, 2010, **51**, 6058–6070.
45 A. Bandyopadhyay, P. K. Valavala and T. C. Clancy, *et al.*, *Polymer*, 2011, **52**, 2445–2452.
46 S. Masoumi, B. Arab and H. Valipour, *Polymer*, 2015, **70**, 351–360.
47 A. Shokuhfar and B. Arab, *J. Mol. Model.*, 2013, **19**, 3719–3731.
48 F. Aghadavoudi, H. Golestanian and Y. Tadi Beni, *Polym. Compos.*, 2017, **38**, E433–E442.
49 S. G. Lee, S. S. Jang and J. Kim, *et al.*, *TADVP*, 2010, **33**, 333–339.
50 J. Mijović and H. Zhang, *J. Phys. Chem. B*, 2004, **108**, 2557–2563.
51 Y. C. Lin and X. Chen, *Chem. Phys. Lett.*, 2005, **412**, 322–326.
52 S. Masoumi and H. Valipour, *Modell. Simul. Mater. Sci. Eng.*, 2016, **24**, 35011.
53 S. Pandiyan, J. Krajniak and G. Samaey, *et al.*, *Comput. Mater. Sci.*, 2015, **106**, 29–37.
54 C. Wu and W. Xu, *Polymer*, 2007, **48**, 5440–5448.
55 D. Xin and Q. Han, *Mol. Simul.*, 2013, **39**, 322–329.
56 L. Tam, D. Lau and C. Wu, *Mol. Simul.*, 2018, 1–9.
57 C. Li and A. Strachan, *Polymer*, 2016, **97**, 456–464.
58 D. Zhang, K. Li and Y. Li, *et al.*, *Soft Matter*, 2018, **14**, 8740–8749.
59 L. L. Marsh, R. Lasky and D. P. Seraphim, *et al.*, *IBM J. Res. Dev.*, 1984, **28**, 655–661.
60 J. Zhou and J. P. Lucas, *Polymer*, 1999, **40**, 5505–5512.
61 LAMMPS: Large-scale Atomic/Molecular Massively Parallel Simulator (https://lammps.sandia.gov/index.html).
62 W. D. Cornell, P. Cieplak and C. I. Bayly, *et al.*, *J. Am. Chem. Soc.*, 1995, **117**, 5179–5197.
63 W. J. Mortier, K. Van Genechten and J. Gasteiger, *J. Am. Chem. Soc.*, 1985, **107**, 829–835.
64 W. L. Jorgensen, J. Chandrasekhar and J. D. Madura, *et al.*, *J. Chem. Phys.*, 1983, **79**, 926–935.
65 H. Frank, *Adv. Chem. Phys.*, 1975, **31**, 1.
66 A. R. Leach, *Molecular Modelling: Principles and Applications*, Pearson/Prentice Hall, Harlow, England, New York, 2001.

67 J. Liu, Z. Liu and S. Yuan, *et al.*, *J. Mol. Struct.*, 2013, **1037**, 191–199.
68 J. Zeng, J. Zhang and X. Gong, *Comput. Theor. Chem.*, 2011, **963**, 110–114.
69 A. U. Ortiz, A. P. Freitas and A. Boutin, *et al.*, *Phys. Chem. Chem. Phys.*, 2014, **16**, 9940–9949.
70 A. D. Wade, L. Wang and D. J. Huggins, *J. Chem. Inf. Model.*, 2018, **58**, 1766–1778.
71 R. E. Skyner, J. B. Mitchell and C. R. Groom, *CrystEngComm*, 2017, **19**, 641–652.
72 E. Kucukpinar and P. Doruker, *Polymer*, 2006, **47**, 7835–7845.
73 L. Banks and B. Ellis, *Polymer*, 1982, **23**, 1466–1472.
74 V. Bellenger, J. Verdu and E. Morel, *J. Polym. Sci., Part B: Polym. Phys.*, 1987, **25**, 1219–1234.
75 J. Mijović and H. Zhang, *J. Phys. Chem. B*, 2004, **108**, 2557–2563.
76 T. Mizuguchi, K. Hagita and S. Fujiwara, *et al.*, *Mol. Simul.*, 2019, **45**, 1437–1446.
77 Y. C. Lin and X. Chen, *Polymer*, 2005, **46**, 11994–12003.
78 P. Nogueira, C. Ramírez and A. Torres, *et al.*, *J. Appl. Polym. Sci.*, 2001, **80**, 71–80.
79 L. Garden and R. A. Pethrick, *J. Appl. Polym. Sci.*, 2017, 134.
80 S. Popineau, C. Rondeau-Mouro and C. Sulpice-Gaillet, *et al.*, *Polymer*, 2005, **46**, 10733–10740.
81 P. W. Atkins, *Quanta: A Handbook of Concepts*, Clarendon Press, 1991.
82 M. Sprik, *J. Chem. Phys.*, 1991, **95**, 6762–6769.
83 C. Brot, G. Bossis and C. Hesse-Bezot, *Mol. Phys.*, 1980, **40**, 1053–1072.
84 O. Gereben and L. Pusztai, *Chem. Phys. Lett.*, 2011, **507**, 80–83.
85 D. Li and G. Jia, *Phys. A*, 2016, **449**, 348–356.
86 D. C. Elton, *Understanding the Dielectric Properties of Water*, PhD thesis, The Graduate School, Stony Brook University, Stony Brook, NY, 2016.
87 M. Neumann, *J. Chem. Phys.*, 1985, **82**, 5663–5672.
88 R. E. Isele-Holder, W. Mitchell and A. E. Ismail, *J. Chem. Phys.*, 2012, **137**, 174107.
89 A. P. Tran, M. R. M. Ardekani and S. Lambot, *Geophysics*, 2012, **77**, H33–H44.
90 D. P. Fernandez, Y. Mulev and A. Goodwin, *et al.*, *J. Phys. Chem. Ref. Data*, 1995, **24**, 33–70.

